RESEARCH ARTICLE

Empirical Characterization and Modeling of the Propagation Channel Inside the VIRC

MHD ZAHER MAHFOUZ [ID][1], **ROBERT VOGT-ARDATJEW** [ID][1], (Member, IEEE),
ANDRÉ B. J. KOKKELER [ID][1], (Member, IEEE), AND
ANDRÉS ALAYÓN GLAZUNOV [ID][1,2], (Senior Member, IEEE)

[1]Faculty of Electrical Engineering, Mathematics and Computer Science, University of Twente, 7500 AE Enschede, The Netherlands
[2]Department of Science and Technology, Linköping University, SE-601 74 Norrköping, Sweden

Corresponding author: Mhd Zaher Mahfouz (z.mahfouz@utwente.nl)

ABSTRACT Over-the-air (OTA) testing and electromagnetic compatibility (EMC) measurements are widely performed in classical reverberation chambers. A less-known reverberation chamber, yet a considerably efficient environment for generating multipath conditions, is the vibrating intrinsic reverberation chamber (VIRC). This article thoroughly investigates the radio propagation channel inside the VIRC. The specific channels studied are narrowband single-input single-output (SISO) systems operating in the frequency range from 670–2740 MHz. A relevant application is OTA testing wireless baseband algorithms or modems for wireless sensor networks, specifically low-power wide-area networks such as Narrowband-IoT (NB-IoT), Long Range (LoRa) and Ultra-Narrowband (UNB). The focus is on the first- and second-order temporal and spectral channel characteristics: coherence time, Doppler spectrum, Doppler spread, frequency autocovariance function, coherence bandwidth, rejection rate of chi-squared goodness-of-fit test for Rician distribution, Rician K-factor, and channel gain. Besides the impact of the frequency of operation, the investigation considers the effect of the rotational speed of the VIRC motors, two loading conditions, on the channel characteristics. An analysis of the measurement results shows that the stirring efficiency degrades while the coherence time increases at slow rotational speeds, with loading, and/or at low frequencies. Moreover, empirical models closely fitting the behavior of various investigated characteristics are proposed, for which we provide foundational physical interpretations. A further investigation is carried out to demonstrate the generality and briefly illustrate the potential usability of these models for both EMC and OTA testing.

INDEX TERMS Coherence bandwidth, coherence time, Doppler, electromagnetic compatibility (EMC), K-factor, over-the-air (OTA), Rayleigh, rejection rate, Rician, vibrating intrinsic reverberation chamber (VIRC).

I. INTRODUCTION

Over-the-air (OTA) testing and electromagnetic compatibility (EMC) measurements are typically performed in rooms shielded from ambient interference. Furthermore, especially at high frequencies, such enclosures are modified to create an environment suitable for the desired test. On the one hand, lining the room with absorbers makes an anechoic chamber

The associate editor coordinating the review of this manuscript and approving it for publication was Deepak Mishra [ID].

that emulates a free-space environment necessary, e.g., for the measurement setups of antenna characterization [1] and wireless coexistence [2]. On the other hand, a resonating and electrically large room creates a reverberation chamber (RC) that emulates a rich multipath environment. Such a chamber has been used in EMC to conduct, e.g., immunity measurements and radiated emission measurements [3]. In the last two decades, nevertheless, RCs have become an indispensable OTA-testing tool in research and development, namely, OTA testing of wireless baseband algorithms [4],

[5], OTA-based antenna measurements [6], [7], [8], and OTA testing of wireless devices (i.e., baseband and antennas combined) [9], [10], [11], [12].

Traditionally, RCs use fixed, rigid metallic walls to build an overmoded rectangular resonant cavity. Such chambers are commonly known as classical reverberation chambers (CLRCs) [13]. Instead, we focus here on a variation of the RC, known as the vibrating intrinsic reverberation chamber (VIRC) [14]. The VIRC walls are made of flexible but reflective (metallic) fabric. There are two fundamental differences between the VIRC and the CLRC. 1) The boundary conditions in the CLRC are altered using at least one rotating mechanical stirrer. In the VIRC, on the other hand, the walls act as mechanical stirrers, which vibrate and alter the boundary conditions. 2) Since the slightest vibration in the VIRC causes unpredictable changes in the field resonance pattern, the mode-tuning technique (a.k.a. stepping stirrers) cannot be implemented in the VIRC. This technique is commonly adopted in the CLRC, e.g., in [10]. On the other hand, the mode-stirring technique (a.k.a. continuously moving stirrers) is alternatively adopted in the VIRC as, e.g., in [15] and [16]. It is usually implemented by air fans or DC motors pushing/pulling randomly on the VIRC fabric [15], [16].

In addition to the advantages of cost-effectiveness and *in-situ* testing, it has been shown that the VIRC can exhibit a performance comparable to that of the CLRC of a similar size [16], [17]. In recent studies, different VIRCs have been investigated in terms of various characteristics [15], [16], [17], [18], [19], [20], [21]: field statistical distribution, field uniformity, Q-factor, K-factor, lowest usable frequency, average mode bandwidth, and the number of collectable independent samples. However, these characteristics are either individually investigated using different VIRC frameworks or not estimated following a VIRC systematic methodology. In [22], a measurement and estimation methodology was recently proposed to characterize the propagation channel inside the VIRC regarding the first- and second-order temporal and spectral characteristics. The literature from [15], [16], [17], [18], [19], [20], [21], and [22] contributes valuable complementing frameworks for analyzing the VIRC. However, these works lack a practical guide for generating a propagation channel with predefined characteristics or establishing hands-on relationships between channel parameters and VIRC variables.

This article, building upon the foundation laid out in [23], addresses these gaps by applying the methodology derived from [22] to a specialized channel behavior. Our proposed practical recipe establishes empirically derived relationships connecting channel characteristics with VIRC variables. Notably, the generality of this approach allows its application to any existing VIRC by adhering to the framework outlined in [22]. This involves conducting radio propagation channel measurements and fitting parameter models to well-known physical characteristics of the radio propagation channel in the VIRC presented in this paper.

TABLE 1. List of abbreviations.

Abbreviation	Definition
AFD	average fade duration
CB	coherence bandwidth
CF	carrier frequency
CLRC	classical reverberation chamber
CT	coherence time
DC	direct current
EMC	electromagnetic compatibility
FS	frequency stirring
LC	loading condition
LCR	level crossing rate
LPWAN	low-power wide-area network
LUF	lowest usable frequency
MAF	moving average filter
MIMO	multiple-input multiple-output
NB	narrowband
NFAF	normalized frequency autocovariance function
NLS	nonlinear least-squares
OTA	over-the-air
PDP	power delay profile
RC	reverberation chamber
RR	rejection rate
RS	rotational speed
SISO	single-input single-output
VIRC	vibrating intrinsic reverberation chamber
VNA	vector network analyzer

The proposed method not only calibrates the measurement setup but also defines the specific applicability limits of the considered VIRC. It is essential to clarify that a comprehensive theoretical treatment of the established empirical relationships lies beyond the scope of this analysis. Nevertheless, we provide a foundational physical interpretation of the presented models. This contribution aims to facilitate practical implementation and understanding, bridging the gap between theoretical frameworks and hands-on applications in VIRC analysis.

To the authors' best knowledge, this is the first systematic and thorough investigation of the VIRC for OTA measurements, including both empirical characterization and modeling, regarding the first- and second-order temporal and spectral characteristics of the radio propagation channel within. The produced radio propagation channel and the investigation thereof are suitable for OTA testing of wireless baseband algorithms in narrowband (NB) single-input single-output (SISO) systems. Nevertheless, given the equivalence between EMC and OTA characteristics in [22, Tab. 1], the investigation also fully applies to EMC. The investigation provides an essential characterization of the propagation channel inside the VIRC. This is useful to understand the statistical properties better and fully utilize the potential capabilities of this unique electromagnetic measurement environment for both EMC and OTA testing.

The main contributions of this article can be summarized as follows.

- We assemble a specialized implementation of the general framework presented in [22], including the

setups of the VIRC and the radio propagation channel. The specific channels studied are narrowband single-input single-output (SISO) systems operating in the frequency range from 670–2740 MHz.

- We thoroughly investigate fundamental statistical characteristics of the SISO radio propagation channel generated within the VIRC.

    1) Second-order temporal characteristics: coherence time, Doppler spectrum, and Doppler spread.
    2) Second-order spectral characteristics: frequency autocovariance function and coherence bandwidth.
    3) First-order characteristics: rejection rate of chi-squared goodness-of-fit test for Rician distribution, Rician K-factor, and channel gain.

The channel parameters are investigated by varying the effect of three independent VIRC variables, i.e., the carrier frequency (CF), the rotational speed (RS) of VIRC motors, and the VIRC loading condition (LC).

- We propose several empirical models to fit the behavior of the following characteristics.

    1) Coherence time as a function of the carrier frequency and the rotational speed.
    2) Doppler spectrum model differentiating stirred and unstirred components contributions.
    3) Frequency autocovariance function.
    4) K-factor versus rotational speed.
    5) Channel gain versus carrier frequency.

We provide foundational physical interpretations of the fitting parameters and their significance for the VIRC channel behavior as a function of VIRC parameters. The empirical equations aim to provide a systematic approach to the reproducibility of the emulated channel behavior under current VIRC and channel settings.

- We verify the validity of the approach presented in [22] by establishing its applicability to different VIRC settings. These include variations in channel parameters and their practical implications.
- We demonstrate the generality of the presented models and illustrate their potential usability for both EMC and OTA testing. We discuss the relevance of the provided fitting models in developing a channel emulator, evaluating the effectiveness of a stirring mechanism, and assessing the radiation efficiency of an antenna under test.

For convenience, a list of abbreviations is provided in Table 1. The remainder of this article is organized as follows. A brief overview of the methodology proposed in [22] and utilized in this article is given in Section II. Section III presents the framework, including the setups of both the channel and the VIRC. The measurement results are presented, analyzed, and discussed in Section IV in which various empirical fitting models are proposed. Section V discusses the validity of the statistical method and demonstrates these models' generality and potential usability. A conclusion and a motivation for future work are given in Section VI.

II. OVERVIEW OF METHODOLOGY

The empirical characterization in this article follows the measurement and estimation methodology proposed in [22]. The VIRC under investigation is connected to a vector network analyzer (VNA) that measures the aggregate S_{21}-parameter between two antennas, including the radio propagation channel. Since the channel is time-variant, this methodology comprises three priority-based investigation steps. Each of them considers the effect of three VIRC variables: the carrier frequency (CF, denoted by f_c), the rotational speed (RS, denoted by ω) of the VIRC motors, and the VIRC loading condition (LC). Any unique combination of values of these variables is referred to as a *configuration* throughout this article. For completeness, the estimation formulas from [22] considered in each of the three investigation steps are summarized in the following three corresponding subsections.

A. SECOND-ORDER TEMPORAL CHARACTERISTICS–METHODOLOGY

To achieve, e.g., a less-than-10% desired accuracy in the coherence time estimation, the normalized time autocovariance function [24] is estimated from 4 uncorrelated realizations, resulting in the 4 estimates [22]:

$$\hat{\rho}_{t,n}(m\Delta t) = \frac{\frac{1}{N}\sum_{k=0}^{N-m-1} s_{21,n}(k\Delta t)\, s_{21,n}^*((k+m)\Delta t) - |c_n|^2}{\frac{1}{N}\sum_{k=0}^{N-1} \left|s_{21,n}(k\Delta t)\right|^2 - |c_n|^2} \tag{1}$$

where $n \in \{1, 2, 3, 4\}$, $c_n = \frac{1}{N}\sum_{k=0}^{N-1} s_{21,n}(k\Delta t)$, $s_{21,n}^*$ is the complex conjugate of $s_{21,n}$, $s_{21,n}(t)$ is the nth collected realization of $S_{21}(t)$, $N = 10^4$ is the number of time samples (i.e., data points) in $s_{21,n}(t)$, $m \in \{0, 1, \ldots, N-1\}$ is the time offset index at which $\hat{\rho}_t$ is evaluated, $\Delta t = T_{\text{swp}} \div N$, and T_{swp} is a variable VNA sweep duration which is dependent on the considered configuration.

Using the estimated autocovariance function, the estimated coherence time (CT) is defined as the minimum positive solution, $\hat{T}_{\text{coh@37\%},n}$, of [22]

$$\left|\hat{\rho}_{t,n}(\hat{T}_{\text{coh@37\%},n})\right| = e^{-1} \tag{2}$$

where $n \in \{1, 2, 3, 4\}$. Furthermore, the estimated Doppler spread is given by [25]

$$\hat{v}_{D,n} = 1/\hat{T}_{\text{coh@37\%},n} \tag{3}$$

The Doppler spectrum is estimated using Bartlett's method from each of the 4 collected realizations, resulting in the 4 estimates [26]:

$$\hat{\mathcal{L}}_n(v) = \frac{1}{L}\sum_{i=1}^{L}\left|\sum_{k=0}^{\frac{N}{L}-1} s_{21,n,i}(k\Delta t)\exp(-j2\pi vk)\right|^2 \tag{4}$$

where $n \in \{1, 2, 3, 4\}$, ν is the Doppler frequency, $L = 5$ is a segmentation factor, $\Delta t = T_{\text{swp}} \div N$, T_{swp} is a variable VNA sweep duration which is dependent on the considered configuration, $N = 10^4$ is the number of time samples (i.e., data points) in $s_{21,n}(t)$, and $s_{21,n,i}(t)$ is the ith segment of the nth collected realization, $s_{21,n}(t)$, of $S_{21}(t)$. Finally, the sample mean (i.e., $\overline{X}$) is computed from (2), (3), and (4) using 4 estimates to obtain $\hat{\overline{T}}_{\text{coh}@37\%}$, $\hat{\overline{\nu}}_D$, and $\hat{\mathcal{L}}(\nu)$, respectively, according to [22].

The longest CT of the slowest-fading case scenario, $T_{\text{coh}}|_{\max}$, is defined for a threshold $= e^{-1} \approx 37\%$ and corresponds to the following configuration: $(f_c|_{\min}, \omega|_{\min}$, fully loaded VIRC). On the other hand, the shortest CT of the fastest-fading case scenario, $T_{\text{coh}}|_{\min}$, is defined for a more conservative threshold $= 90\%$ and corresponds to the following configuration: $(f_c|_{\max}, \omega|_{\max}$, unloaded VIRC). In the next two investigation steps, $T_{\text{coh}}|_{\min}$ and/or $T_{\text{coh}}|_{\max}$ are essential [22].

B. SECOND-ORDER SPECTRAL CHARACTERISTICS–METHODOLOGY

To achieve, e.g., a less-than-35% desired accuracy in the coherence bandwidth estimation, the normalized frequency autocovariance function (NFAF) [24] is estimated from 4×125 uncorrelated realizations, and it is given by [22]

$$\hat{\rho}_{f,n}(\Delta f) = \frac{\hat{\mathbb{C}}\left[s_{21,a_n:b_n}\left(-\frac{\text{BW}}{2}\right), s_{21,a_n:b_n}\left(-\frac{\text{BW}}{2} + \Delta f\right)\right]}{\hat{\mathbb{S}}\left[s_{21,a_n:b_n}\left(-\frac{\text{BW}}{2}\right)\right]\hat{\mathbb{S}}\left[s_{21,a_n:b_n}\left(-\frac{\text{BW}}{2} + \Delta f\right)\right]} \tag{5}$$

where $n \in \{1, 2, 3, 4\}$, $\Delta f \in [0, \text{BW}]$ is the frequency offset at which $\hat{\rho}_f$ is evaluated, $a_n = 1 + (n-1)D$, $b_n = nD$, $s_{21,a_n:b_n}(f)$ is the nth group of $D = 125$ collected realizations of $S_{21}(f)$, BW is a variable VNA span that is dependent on the considered configuration, whereas the two unbiased estimators, $\hat{\mathbb{C}}$ and $\hat{\mathbb{S}}$, are the sample covariance and the sample standard deviation, respectively.

Using the estimated NFAF, the estimated coherence bandwidth (CB) is defined as the minimum positive solution, $\hat{B}_{\text{coh}@37\%}$, of [22]

$$\left|\hat{\rho}_{f,n}(\hat{B}_{\text{coh}@37\%,n})\right| = e^{-1} \tag{6}$$

where $n \in \{1, 2, 3, 4\}$. Finally, the sample mean (i.e., $\overline{X}$) is computed from (5) and (6) using 4 estimates to obtain $\hat{\overline{\rho}}_f$ and $\hat{\overline{B}}_{\text{coh}@37\%}$, respectively, according to [22].

The largest CB, $B_{\text{coh}}|_{\max}$, among all possible configurations of $(f_c, \omega$, fully loaded VIRC) is defined for a threshold $= e^{-1} \approx 37\%$. $B_{\text{coh}}|_{\max}$ is essential for the frequency-stirring (FS) technique in the next investigation step [22]. On the other hand, the smallest CB, $B_{\text{coh}}|_{\min}$, among all possible configurations of $(f_c, \omega$, unloaded VIRC) is defined for a more-conservative threshold $= 90\%$. Given the scope of this article, $B_{\text{coh}}|_{\min}$ is used to determine the upper limit on the signaling rate of NB systems for OTA
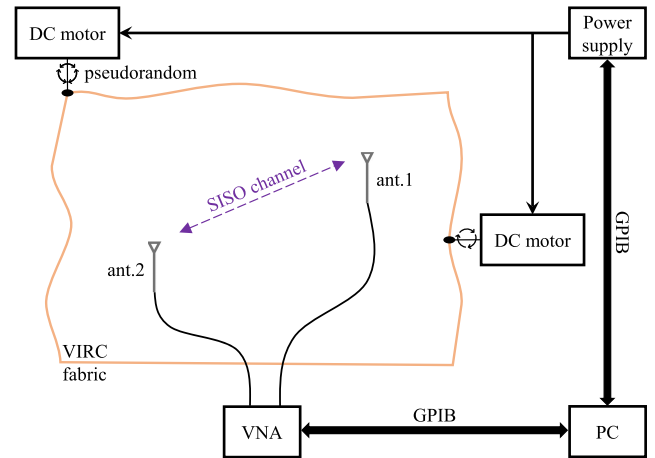

FIGURE 1. Schematic illustration of the framework.

testing in the VIRC. By definition, an NB system experiences flat fading when it is deployed in an intended real-world environment. Thus, such an NB system will experience the desired flat fading when it is tested in the VIRC as long as its signaling rate is less than $B_{\text{coh}}|_{\min}$.

C. FIRST-ORDER CHARACTERISTICS–METHODOLOGY

To be able to estimate an unknown K-factor, e.g., as low as -35 dB with an expected bias of up to 1.5 dB and an expected confidence interval whose width is up to 6.5 dB, $M = 10^4$ uncorrelated realizations are collected [22]. Moreover, a four-tap moving average filter (MAF) is adopted for FS [22].

The rejection rate (RR) of the chi-squared[1] goodness-of-fit test for Rician distribution is estimated from [22]

$$\hat{R} = \left\langle \frac{1}{\eta} \sum_{n=0}^{\eta-1} D_{H_0}\left\{s_{21,a_n}, \ldots, s_{21,b_n}\right\} \right\rangle_{\text{FS}} \tag{7}$$

where $\langle \cdot \rangle_{\text{FS}}$ is the output of the FS MAF over the adjacent frequency samples (i.e., data points), $\eta = 10$ tests per configuration, $a_n = 1 + n\gamma$, $b_n = (1 + n)\gamma$, $\gamma = M \div \eta = 1000$ data points per test per configuration, and D_{H_0} is the outcome of the test decision for the null hypothesis, H_0, that the measurement dataset, $\{s_{21,a_n}, \ldots, s_{21,b_n}\}$, is drawn from a theoretical Rician distribution.

The K-factor is estimated using the biased estimator [22]:

$$\hat{K} = \left\langle \frac{|\overline{S_{21}}|^2}{\overline{|S_{21} - \overline{S_{21}}|^2}} \right\rangle_{\text{FS}} \tag{8}$$

---

[1] In [27], it is mentioned that the chi-squared test is not well adapted to the case of a continuous distribution, which is the case of RC measurements. However, the authors in [28] argued that the chi-squared test's performance depends crucially on how the data is binned. By proposing a binning method, they demonstrated that it is generally competitive and sometimes even superior to other tests, including the Anderson-Darling test. Additionally, in practical measurements, since the parameters of the estimated cumulative distribution function are not known a priori, the chi-squared test is more suitable compared to the Anderson-Darling test since the latter requires the cumulative distribution function to be completely specified [29].

TABLE 2. VIRC variables and their considered configurations.

Section	Carrier frequency (MHz)	Rotational speed (r/min)	Loading condition
IV-A	{868, 2458}	{19.4, 21.4, 24.8, 28.3, 32.1, 35.9, 39.5, 42.9}	unloaded
	{670, 720, 770, 820, 868, 1200, 1500, 1800, 2100, 2458, 2740}	{19.4, 28.3, 42.9}	unloaded
	{868, 2458}	{19.4, 28.3, 42.9}	loaded
IV-B	{670, 720, 770, 820, 868, 1200, 1500, 1800, 2100, 2458, 2740}	{19.4, 28.3, 42.9}	unloaded
	{670, 720, 770, 820, 868, 1200, 1500, 1800, 2100, 2458, 2740}	{19.4, 28.3, 42.9}	loaded
IV-C	[670–2740]	{19.4, 21.4, 24.8, 28.3, 32.1, 35.9, 39.5, 42.9}	unloaded
	[670–2740]	{19.4, 28.3, 42.9}	loaded

where $\overline{S_{21}}$ is the sample mean of S_{21}. Finally, the estimated channel gain (a.k.a. average power transfer level) is given by the following unbiased estimator [30]:

$$\hat{G} = \left\langle \overline{|S_{21}|^2} \right\rangle_{\text{FS}} \tag{9}$$

III. FRAMEWORK AND MEASUREMENT SETUP

A schematic illustration of the framework shown in Fig. 1 depicts a SISO channel between two antennas inside the VIRC. An Agilent N5230A measures the aggregate S_{21}-parameter. The framework, which incorporates the setups of both the channel and the VIRC, is an essential step for future work concerning developing a channel emulator for low-power wide-area networks (a.k.a. LPWANs). Therefore, the aim has been originally set to assemble a simple, cost-effective setup capable of providing a near-Rayleigh channel and supporting the 868 MHz and 2.4 GHz license-free bands.

In the following subsections, the structure of the VIRC under investigation and the components of the channel inside are described and justified. The settings of the measurement setup of both the VIRC variables and the VNA are also listed.

A. VIRC SETUP

The VIRC is located at the lab of the Power Electronics & EMC research group at the University of Twente. An exterior view of the VIRC with dimensions 1.0 m × 1.2 m × 1.5 m is shown in Fig. 2. Its walls are made of a copper fabric, which delimits the volume of the chamber. Moreover, its front wall is fixed to a metal frame to which a hatch is attached. The rest of the fabric is tied only with strings and springs to the frame. Their purpose is to maintain the rectangular geometry while providing enough flexibility to ensure unrestrained operation of the DC motors shown in Fig. 2.

Each motor has an arm that pulls the flexible fabric, causing it to wrinkle on the whole surface. As a result, different boundary conditions for the resonant field within the chamber are continuously created. One of the motors is attached to the corner of the VIRC. In this way, all three walls are directly engaged in the stirring while maintaining the average volume of the chamber. This motor also pseudo-randomly changes its direction every 0.2–2.0 s. This causes the fabric to wrinkle differently each time. Along with a continuously rotating second motor, such a VIRC setup ensures that all five walls simultaneously

vibrate. This positively contributes to the effectiveness of the stirring mechanism by continually creating unpredictably new boundary conditions for a long time [15], [16].

B. CHANNEL SETUP

According to the preliminary investigation in [22], the VIRC under investigation is slightly preloaded to lower the RR of its channel envelope histogram. As can be seen in Fig. 3, the interior side of the hatch carries a 2 × 2 pyramidal carbon foam absorber whose dimensions are 20 cm × 16 cm × 16 cm (H × W × L). It should be noted that this slight preloading is not referred to as "loaded" in the context of LC.

An interior view of the VIRC is shown in Fig. 4. Two broadband omnidirectional antennas are adopted. Their matching efficiency is plotted in Fig. 6. Furthermore, the VIRC can be seen loaded with two 1 × 6 pyramidal carbon foam absorbers whose dimensions are 30 cm × 10 cm × 60 cm (H × W × L).

The top and side views of the layout inside the VIRC are depicted in Fig. 5. To achieve a very small K-factor in RCs, the direct coupling between the two antennas has to be minimized, as their separation distance has to be maximized [10, eq. (13)]. For the former case, the two antennas are cross-polarized [10], [11], see Fig. 4. For the latter case, however, a minimum distance of a quarter wavelength between each antenna and a nearby boundary condition should still be respected. In this framework, we opt for a separation distance, d_i, of at least a half wavelength for all cases.

C. VIRC VARIABLES AND VNA SETTINGS

To investigate the dynamic range of the VIRC characteristics under investigation, different configurations of the VIRC variables (i.e., CF, RS, and LC) are considered. They are summarized in Table 2 for each of the three investigation steps. Regarding the several combinations of RSs and LCs, the focus is on two CFs, i.e., 868 MHz and 2458 MHz. An RS below 19.4 r/min severely degrades the effectiveness of the stirring mechanism. Two LCs are considered: unloaded and loaded. For the latter case, the VIRC is loaded with two 1 × 6 absorbers as seen in Fig. 4 and depicted in Fig. 5.
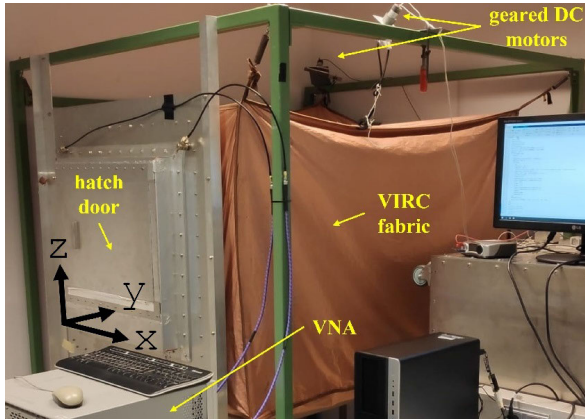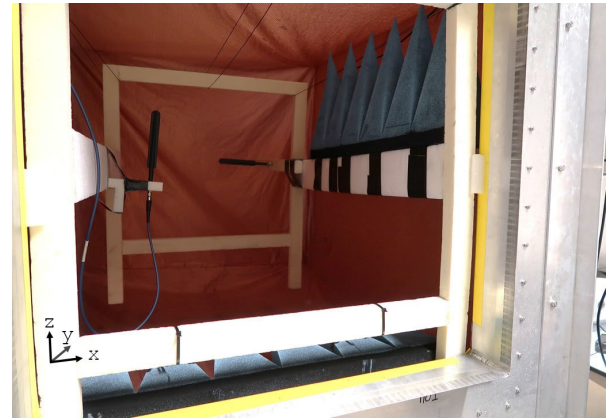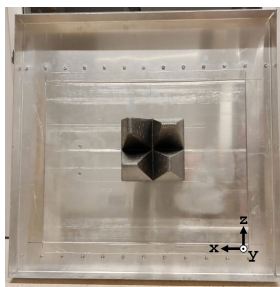
FIGURE 2. Exterior view of the VIRC.

FIGURE 3. Absorber mounted on the interior side of the VIRC hatch as a slight preloading [22]. This preloading is not referred to as "loaded" in the context of LC.

TABLE 3. VNA settings.

VNA parameter	Section		
	IV-A [†]	IV-B [‡]	IV-C [§]
sweep type	zero span	freq. sweep	freq. sweep
center freq.	see CF in Table II	see CF in Table II	-
span	-	(15, 30) MHz [#]	-
start freq.	-	-	670 MHz
stop freq.	-	-	2740 MHz
sweep time	$\geq$ 2500 CTs [¶]	1.5 ms	5.5 ms
No. of points	10^4	27	100
IF bandwidth	1 kHz	20 kHz	20 kHz
trigger cycle	-	1.4 s	1.4 s
No. of sweeps	4	500	10^4

[†] The settings follow from a 95%-confidence level, a less-than-10% desired accuracy in the coherence time estimation, and a VNA buffer size of 20,001 data points [22].

[‡] The settings follow from a 95%-confidence level and a less-than-35% desired accuracy in the coherence bandwidth estimation [22].

[§] The settings follow from a 1.5 dB upper-limit on the expected bias of the estimated K-factor and from a 6.5 dB upper-limit on the width of the expected 95%-confidence interval of the estimated K-factor, given an unknown true K-factor as low as -35 dB and a four-tap FS MAF [22].

[¶] Actual value depends on CF, RS, and LC [22].

[#] Corresponds to (unloaded, loaded) VIRC.
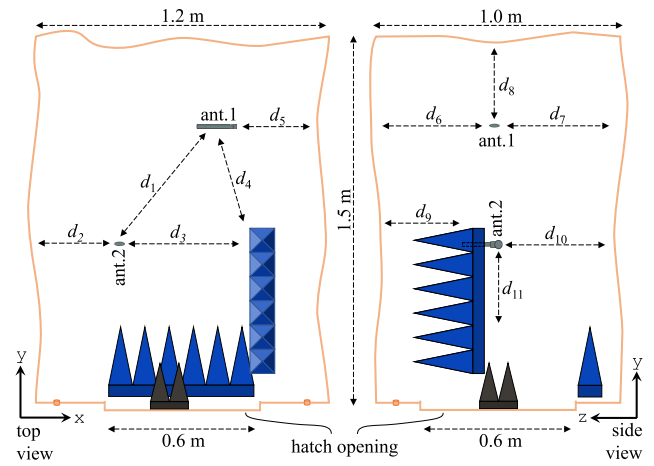

FIGURE 4. Interior view of the VIRC.

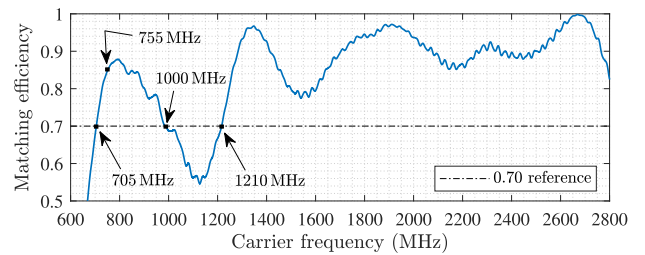FIGURE 5. Top and side views of the layout inside the VIRC.

FIGURE 6. Matching efficiency $(1 - |S_{11}|^2)$ of the utilized identical antennas measured in the anechoic chamber, where S_{11} is the antenna return loss.

TABLE 4. Estimation of the essential primary characteristics.

Characteristic	Configuration	Estimation
$T_{\text{coh}}|_{\min}$	(2740 MHz, 42.9 r/min, unloaded)	5.7 ms
$T_{\text{coh}}|_{\max}$	(670 MHz, 19.4 r/min, loaded)	330 ms
$B_{\text{coh}}|_{\max}$	(f_c, ω, loaded)	20.7 MHz

Table 3 summarizes the VNA settings for the measurement setups of each of the three investigation steps. The estimation results of $T_{\text{coh}}|_{\min}$, $T_{\text{coh}}|_{\max}$, and $B_{\text{coh}}|_{\max}$, which were introduced in Section II, are summarized in Table 4. According to [22], these three primary characteristics are essential—among others—for determining part of the VNA settings.

IV. RESULTS, ANALYSIS AND MODELING

The measurement data is collected according to Section II, and from which the estimations are calculated using (1)–(9). In this section, the measurement results are presented, analyzed, and discussed in detail in the following three subsections. Each of them is dedicated to a different order and/or category of channel characteristics. Moreover, various empirical fitting models are proposed. A foundational physical interpretation of the models is provided.

A. SECOND-ORDER TEMPORAL CHARACTERISTICS–RESULTS

1) COHERENCE TIME

For all the considered configurations listed in Table 2, $\overline{\hat{T}}_{\text{coh@37\%}}$ is plotted as a function of the CF and the RS in Figs. 7(a) and (b), respectively. As the figures indicate, the achievable dynamic range of the CT is 25–250 ms for the VIRC under investigation, which can be tuned to by setting the VIRC configurations accordingly.

Moreover, the expected trend of an inverse-proportionality relation between the CT and the CF can be observed in Fig. 7(a). A similar trend with respect to the RS can also be observed in Fig. 7(b). Consequently, the CT of the VIRC can

be empirically modeled as in

$$T_{\text{coh@37\%}} = \frac{k_1}{f_c} \tag{10}$$

$$T_{\text{coh@37\%}} = \frac{k_2}{\omega} \tag{11}$$

where $T_{\text{coh@37\%}}$ and f_c are expressed in ms and MHz, respectively, k_1 is a unitless constant whose value depends on the RS and the LC, whereas ω is the RS expressed in r/min, and k_2 is a constant expressed in ms $\cdot$ r/min and whose value depends on the CF and the LC.

The nonlinear least-squares (NLS) regression method is used to fit (10) and (11) with $\overline{\hat{T}}_{\text{coh@37\%}}$ of each of the 7 scenarios considered in Figs. 7(a) and (b). All the empirical fits are shown in the same figures. It is worth observing that both (10) and (11) produce good fits as long as the CF and the RS are above 868 MHz and 28.3 r/min, respectively, for the VIRC under investigation.

A foundational physical interpretation is straightforward. Indeed, as is well-known, the CT measures the signal fading decorrelation as an inverse function of the Doppler frequency, which depends on the CF. Hence, the larger the CF, while keeping constant the antenna's and/or scatterers' speed, the larger the Doppler frequency and hence the smaller the CT because fading becomes faster. Similarly, at a fixed frequency, when the speed increases, the Doppler frequency increases, and, therefore, the CT reduces with the RS as expected. The increase of the CT with LC as shown in Fig. 7(b) can be interpreted as the reduction of multipath components contributing to the total fading field as a result of absorption in the loads. This is in accordance with [15], causing both fitting constants to increase. The constants k_1 and k_2 are, therefore, in general, not constant. They depend on the specific VIRC and, as shown on Fig. 7 on the other VIRC variables. Indeed, since the channel is time-variant, increasing the RS causes k_1 to decrease. On the other hand, k_2 decreases when the CF increases, which is typical for wireless channels [25].

2) DOPPLER SPECTRUM AND DOPPLER SPREAD

Four examples of $\overline{\hat{\mathcal{L}}}(\nu)$ are shown in Figs. 8(a)–(d). They correspond to four different configurations, representing—in order—the worst empirical fit, the best empirical fit, and the effect of low and high CFs on the deformation of the Doppler spectrum. As the figures depict, the unstirred component manifests itself as a spike in the middle. This indicates no mean Doppler shift as expected since both antennas are static. Moreover, the magnitude of this spike relative to the skirt indicates how large/small the K-factor is [26] for the considered configuration. On the other hand, the stirred components are represented by the skirt, whose width is proportional to the Doppler spread. Given the latter is defined in this article according to (3), it has been found that 98% of the average power in the *stirred components* is roughly contained within $2 \times \overline{\hat{\nu}}_D$ around the middle of the Doppler spectrum, where $\overline{\hat{\nu}}_D$ is computed by (3). Additionally, the
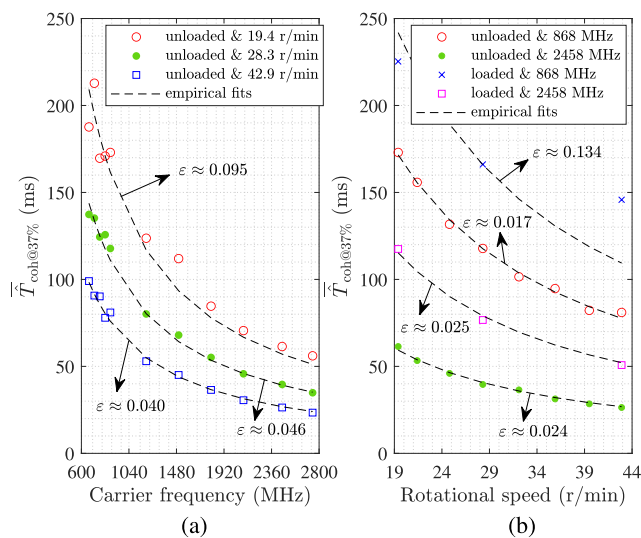

FIGURE 7. Estimated coherence time versus (a) the carrier frequency and (b) the rotational speed. Where ε is the coefficient of variation of the root-mean-square error between $\overline{\hat{T}}_{\text{coh@37\%}}$ and empirical fits.
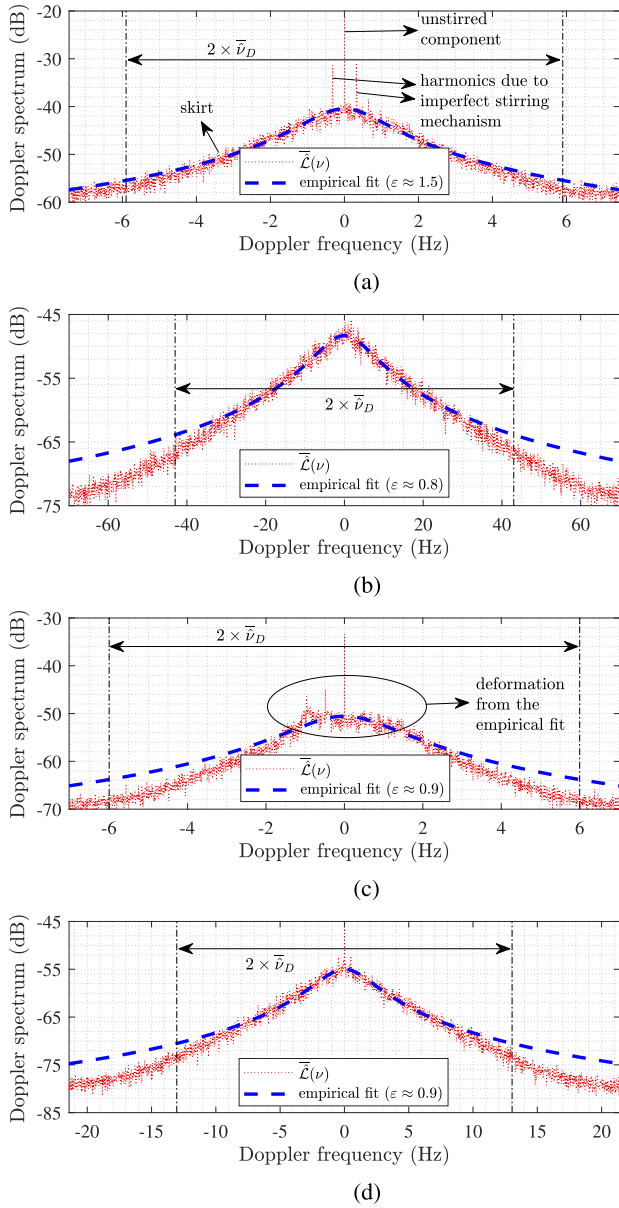
FIGURE 8. Estimated Doppler spectrum of the configurations:
(a) (770 MHz, 19.4 r/min, unloaded), (b) (2740 MHz, 42.9 r/min, unloaded),
(c) (868 MHz, 28.3 r/min, loaded), and (d) (2458 MHz, 28.3 r/min, loaded).

symmetric feature of the Doppler spectrum of the unloaded VIRC in Figs. 8(a) and (b) is an indication that the stirred components arrive uniformly from all directions. However, the two harmonics can be observed in Fig. 8(a) is an indication of a poor stirring efficiency. This can be attributed to the combined effect of a limited mode density at a low CF of 770 MHz and an imperfection in the stirring mechanism at a very slow RS of 19.4 r/min. The latter effect is discussed further in Section IV-C2.

According to [31], the Bell shape (a.k.a. inverted-V shape in decibel scale) is proposed as a channel model for the Doppler spectrum of IEEE 802.11 fixed indoor SISO links. When the mode-stirring technique is adopted in CLRCs, the inverted-V shape emerges in many scenarios [26], [32],
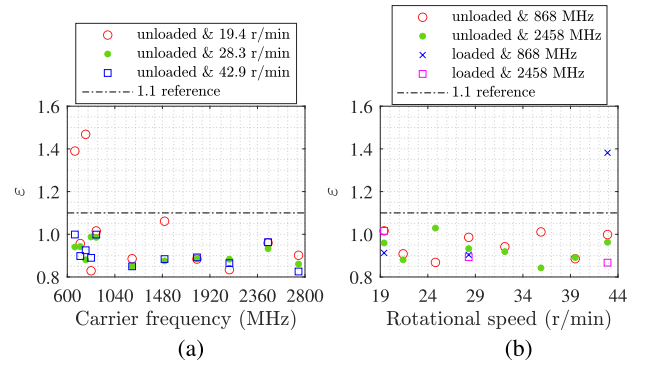

FIGURE 9. The goodness-of-fit of (12) versus (a) the carrier frequency and (b) the rotational speed.

[33], [34], [35]. This trend is also true here in the VIRC as, e.g., Figs. 8(a)–(d) show. Consequently, considering the *stirred components* exclusively, the Doppler spectrum of the VIRC can be empirically modeled in linear values as in [31]

$$\mathcal{L}(\nu) = \frac{k_3}{1 + 35\left(\dfrac{\nu}{k_4}\right)^2} \tag{12}$$

where ν is expressed in Hz, k_3 is a unitless constant whose value mainly depends on the CF and LC, whereas k_4 is a constant expressed in Hz and whose value is dependent on all the three VIRC variables. It is worthwhile to note that while full physical modeling of the Doppler spectrum is outside the scope of this study, the shape of the spectrum is similar to the one proposed in [36] and [37], where the Bell shape of the Doppler spectrum is explained by antennas not moving relative to each other while scattering/reflections taking place at both the transmitter and receiver. In our case, the scatterers are the undulating walls of the VIRC.

The NLS regression method is used to fit (12) with $\overline{\hat{\mathcal{L}}}(\nu)$ of the *stirred components*. The empirical fits are shown in the same corresponding figures of $\overline{\hat{\mathcal{L}}}(\nu)$, i.e., Figs. 8(a)–(d). To compare the goodness-of-fit among the considered configurations, the coefficient of variation, ε, of the root-mean-square error between $\overline{\hat{\mathcal{L}}}(\nu)$ and (12) is used. The coefficient is calculated by normalizing the root-mean-square error to the mean, i.e., to the power of the *stirred components*. This normalization guarantees a fair comparison. For all the considered configurations listed in Table 2, ε is calculated in linear values and graphically presented in Figs. 9(a) and (b) as a function of the CF and the RS, respectively. Considering the unloaded VIRC, most configurations have a good fit whose ε is in the range 0.8–1.1. However, for low CFs and very slow RSs, ε becomes greater than 1.4. The worst (i.e., $\varepsilon \approx 1.5$) and the best (i.e., $\varepsilon \approx 0.8$) fits are shown in Figs. 8(a) and (b), respectively. In the former case, the bad fit can be attributed to the two harmonics above. Considering the loaded VIRC, on the other hand, it is worth mentioning that the validity of (12) is questionable for low CFs regardless of the RS or how small ε is. A deformation from the empirical fit can be observed in Fig. 8(c) which corresponds to the
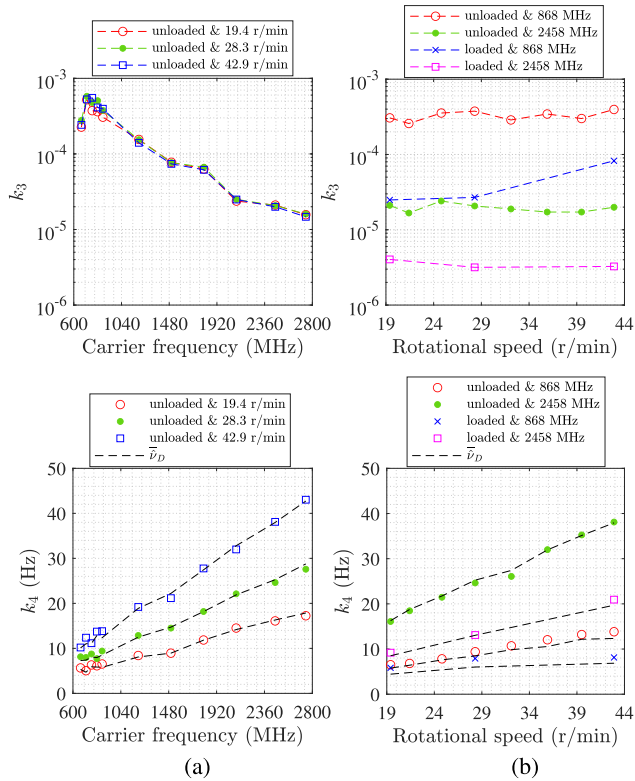
FIGURE 10. Fitting constants, k3 and k4, of (12) versus (a) the carrier frequency and (b) the rotational speed.

configuration (868 MHz, 28.3 r/min, loaded) whose $\varepsilon \approx 0.9$. However, a good fit can still be achieved in case of high CFs such as in Fig. 8(d) which corresponds to the configuration (2458 MHz, 28.3 r/min, loaded) whose $\varepsilon \approx 0.9$.

A foundational physical interpretation of the fitting constants, k_3 and k_4, of (12) can be inferred from a modified analysis presented in [31]. They are graphically presented in Figs. 10(a) and (b) as a function of the CF and the RS, respectively, for all the considered configurations listed in Table 2. According to [31], k_4 is directly proportional to $\bar{\hat{v}}_D$. The constant of this proportionality is empirically set to unity by using a scaling factor of 35 in (12) for the VIRC under investigation. Hence, k_4 can be physically interpreted to model the Doppler spread in the VIRC, which changes as a function of its variables as established by the dependence shown in Figs. 10(a) and (b). Moreover, both k_4 and $\bar{\hat{v}}_D$ closely resemble a straight line as anticipated from (3), (10) and (11). However, as k_4 in Fig. 10(b) indicates, one exception is the configuration of 868 MHz and loaded VIRC, regardless of the RS. This is the result of the aforementioned deformation in the VIRC under investigation. On the other hand, considering Fig. 10(a), k_3 decreases when the CF increases as anticipated from the gain of a typical propagation channel. This is true because the physical interpretation of k_3 is that it represents the power of the *stirred components* as can be indicated from (12). Furthermore, considering k_3 as a

function of the RS in Figs. 10(a) and (b), the former is roughly constant and, thereby, not dependent on the latter. This is true because the RS affects the stirring efficiency rather than the channel gain, as explained further below in Section IV-C3.

B. SECOND-ORDER SPECTRAL CHARACTERISTICS—RESULTS

1) NORMALIZED FREQUENCY AUTOCOVARIANCE FUNCTION

For all the considered configurations listed in Table 2, $|\bar{\rho}_f|$ is plotted in Figs. 11(a) and (b) for the unloaded and the loaded VIRC, respectively. According to the theory [38] and the measurements [39], the linearly scaled power delay profile (PDP) of CLRCs is commonly modeled as an exponentially decaying pulse with a specific time constant that describes how quickly the energy dissipates in the chamber. Moreover, a Fourier-transform pair between the NFAF and the PDP exists. Consequently, the NFAF of the VIRC can be empirically modeled as in

$$|\rho_f| = \frac{1}{\left|1 + j2\pi \dfrac{\Delta f}{k_5}\right|} \tag{13}$$

where k_5 is a frequency constant whose value depends on the LC and the considered CF range. The physical interpretation of $k_5/2\pi$ is known as the half-power coherence bandwidth of the channel. In this paper, instead of this 50% coherence bandwidth, we study the bandwidths defined at the 37% and the 90% power levels of the peak [22].

Before fitting (13) with $\bar{\rho}_f$, the latter is first averaged over the considered CFs (i.e., $\langle \cdot \rangle_{CF}$), then over the considered RSs (i.e., $\langle \cdot \rangle_{RS}$), resulting in the two averages, $\left| \left\langle \bar{\rho}_{f,\text{unloaded}} \right\rangle_{CF,RS} \right|$ and $\left| \left\langle \bar{\rho}_{f,\text{loaded}} \right\rangle_{CF,RS} \right|$, for the unloaded and the loaded VIRC, respectively. Next, the NLS regression method is used to individually fit (13) with these two resulting averages. Both fits are shown in Fig. 11. It is worth observing that (13) produces a good fit as long as the CF and the RS are above 770 MHz and 28.3 r/min, respectively, for the VIRC under investigation. Moreover, loading the VIRC causes k_5 to increase, which is in accordance with [10], since it is directly proportional to the average mode bandwidth.

2) COHERENCE BANDWIDTH

For all the considered configurations listed in Table 2, both $\bar{B}_{\text{coh@37\%}}$ and $\bar{B}_{\text{coh@90\%}}$ are plotted in Figs. 12(a) and (b), respectively, as a function of the CF. As can be observed in the figures, the CB increases due to loading, which is in accordance with [40] and [41]. Additionally, it is roughly flat over the CFs above 820 MHz for the VIRC under investigation. It also has no well-defined behavior when it comes to the RS. This is generally in accordance with [40] and [41] in which the measurements are smoothed using an FS MAF, resulting in an approximately flat behavior. Moreover,
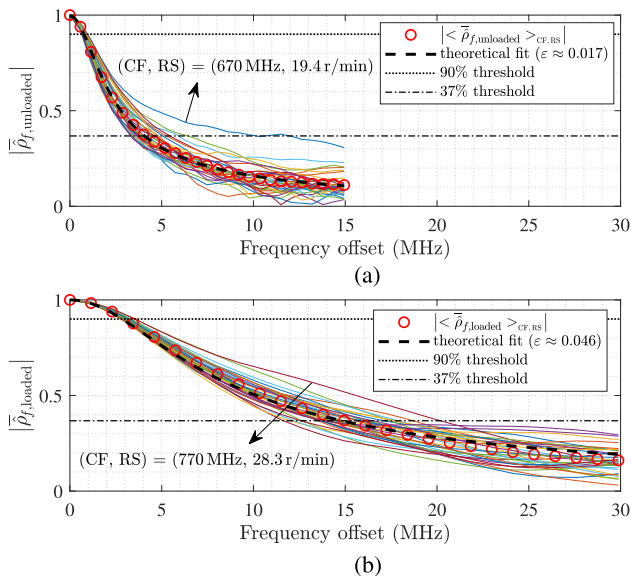
FIGURE 11. Estimated normalized frequency autocovariance function for (a) the unloaded and (b) the loaded VIRC. Solid lines with different colors represent the different configurations. Where ε is the coefficient of variation of the root-mean-square error between $\left|\left\langle \overline{\hat{\rho}_f} \right\rangle\right|$ and empirical fits.

FIGURE 12. Estimated coherence bandwidth defined at (a) 37% and (b) 90% versus the carrier frequency.

for the VIRC under investigation, the upper limit on the signaling rate of NB systems is $B_{\text{coh}}|_{\min} \approx 0.5\,\text{MHz}$, which can be determined from the unloaded VIRC in Fig. 12(b).

C. FIRST-ORDER CHARACTERISTICS—RESULTS

1) REJECTION RATE

The estimated RR of the unloaded and the loaded VIRC are denoted by $\hat{R}_{\text{unloaded}}$ and $\hat{R}_{\text{loaded}}$, respectively. For all the considered RSs listed in Table 2, both $\hat{R}_{\text{unloaded}}$ and $\hat{R}_{\text{loaded}}$ are plotted in Figs. 13(a) and (b), respectively, as a function of the CF. For both LCs, the CFs below 770 MHz have a high $\hat{R}$ well above a 20% reference for the VIRC under investigation. This is due to the limited mode density as reasoned in [42]. Moreover, for the unloaded VIRC specifically, the CF range 930–1220 MHz also has a high $\hat{R}_{\text{unloaded}}$. However, on the contrary to the CFs below 770 MHz, this high $\hat{R}$ is due to the matching efficiency of the utilized antennas that is less than 0.7 within the said frequency range as reasoned in [43]. The high $\hat{R}$ for the two previous cases is true regardless of the RS. Yet, in the case of the loaded VIRC, the same CF range 930–1220 MHz has an $\hat{R}_{\text{loaded}}$ below 20% due the increase in the modal overlap after loading [44]. On the other hand, in case of low CFs and very slow RSs, loading will not help lower its RR as can be indicated from Fig. 13(b) for CFs below 1000 MHz for the VIRC under investigation. Nevertheless, the typical VIRC trend of a low RR below 20% for high CFs [15], [16] can be observed in Figs. 13(a) and (b) regardless of the RS or the LC. Additionally, another trend of an RR decrease as the RS increases can be observed in Fig. 14(b), which is interestingly not true for the unloaded VIRC, as Fig. 14(a) indicates.
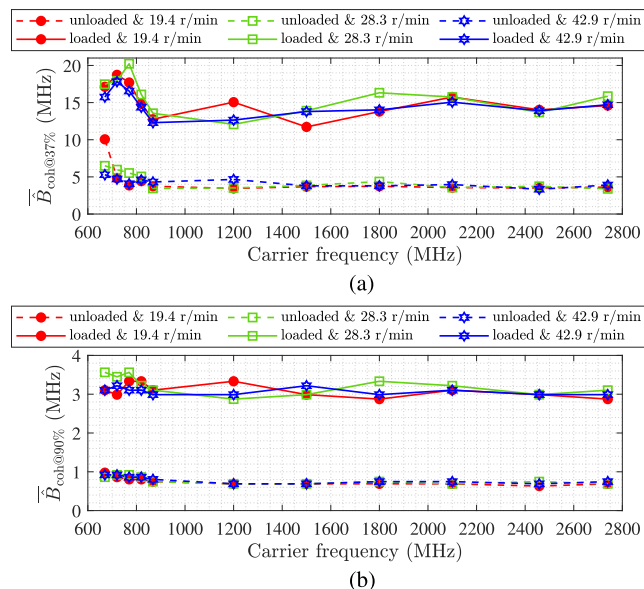
2) K-FACTOR

The estimated K-factor of the unloaded and the loaded VIRC are denoted by $\hat{K}_{\text{unloaded}}$ and $\hat{K}_{\text{loaded}}$, respectively. For all the considered RSs listed in Table 2, both $\hat{K}_{\text{unloaded}}$ and $\hat{K}_{\text{loaded}}$ are plotted in Figs. 15(a) and (b), respectively, as a function of the CF. For the unloaded VIRC under investigation, $\hat{K}_{\text{unloaded}}$ in most of the CF range above 820 MHz is well below $-10\,\text{dB}$. For the loaded VIRC, on the other hand, $\hat{K}_{\text{loaded}}$ in most of the CF range above 1000 MHz is well below $-7\,\text{dB}$, whereas it is only well below $-10\,\text{dB}$ for most of the CF range above 1800 MHz. Moreover, a trend that the K-factor decreases as the CF increases can be seen in the figures for both LCs, which is in accordance with [16], since the VIRC is good at stirring the high CFs. However, no simple relation between $\hat{K}$ and the CF can be observed. This is true because the theoretical formula of the K-factor [10, eq. (13)] is dependent—among others—on two variables: the directivities of the utilized antennas in the direction of each other (which themselves are dependent on the CF) and the average mode bandwidth (hence the LC). The latter has a complicated relation to the CF [10, eq. (7)], which further explains the rapid spectral variations in $\hat{K}$ that can be seen in Figs. 15(a) and (b). Additionally, $\hat{K}$ of different RSs do not overlap, as the figures clearly show. This can be attributed to an imperfection in the stirring mechanism, as explained in the next paragraph. Nevertheless, a compelling correlation between the curves regarding their behavior with respect to the CF can be observed for both LCs in Fig. 15.

According to the theory [10, eqs. (7) and (13)], the K-factor of an RC is dependent on the chamber volume, the directivities of the utilized antennas in the direction of each other, the distance between them, the average mode
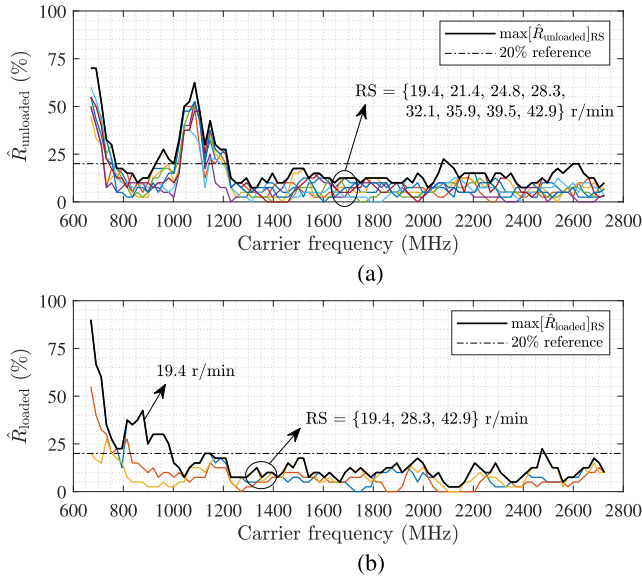
FIGURE 13. Estimated rejection rate versus the carrier frequency for (a) the unloaded and (b) the loaded VIRC. Solid lines with different colors represent the different rotational speeds.
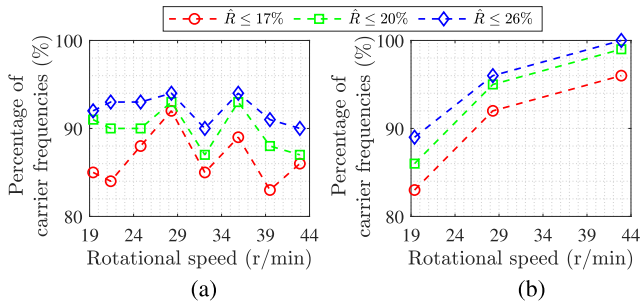

FIGURE 15. Estimated K-factor versus the carrier frequency for (a) the unloaded and (b) the loaded VIRC. Solid lines with different colors represent the different rotational speeds.

FIGURE 14. Percentage of the carrier frequencies at which the estimated rejection rate is below some upper limit versus the rotational speed for (a) the unloaded and (b) the loaded VIRC.

bandwidth, the effectiveness of the stirring mechanism, the CF, and the LC. In this article, we define an intrinsic K-factor, $K_{intrinsic}$, that is independent of the effectiveness of the stirring mechanism. In other words, the actual K-factor of an RC matches its $K_{intrinsic}$ if its stirring mechanism is ideal; hence the latter is a conceptual metric. This concept of $K_{intrinsic}$ can be applied to the VIRC as follows. Considering any point on the VIRC wrinkled fabric, the peak-to-peak displacement along the surface norm depends on the RS due to the inertia effect. This displacement is also known as the shaking amplitude according to [17] and [45]. That means at faster RSs, the VIRC fabric vibrates more significantly. However, at a certain fast RS, the displacement reaches its maximum value due to the physical limitation of the VIRC fabric. Therefore, fast RSs create new uncorrelated boundary conditions and, thereby, cause the actual K-factor of the VIRC to decrease while approaching its $K_{intrinsic}$. At very slow RSs, on the other hand, the displacement reaches its minimum, creating new yet partially correlated boundary
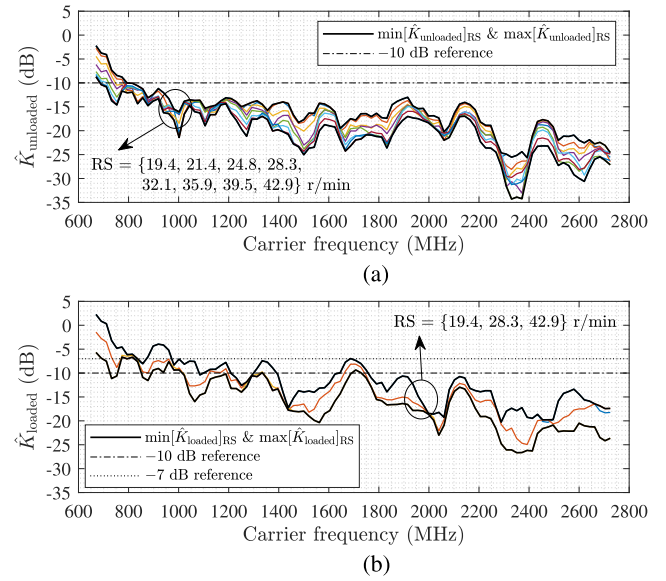
conditions and, thereby, causing the actual K-factor to rather increase above $K_{intrinsic}$.

For the whole range of the CF considered in Table 2, both $\hat{K}_{unloaded}$ and $\hat{K}_{loaded}$ are plotted in Figs. 16(a) and (b), respectively, as a function of the RS. The concept of $K_{intrinsic}$ can be used to explain why $\hat{K}$ of different RSs do not overlap (see Fig. 15), but rather decrease as the RS increases (see Fig. 16). Consequently, after the K-factor of the VIRC is averaged over the considered CFs, it can be empirically modeled in decibels as in

$$\left| \langle K \rangle_{CF} \right|_{dB} = k_6 + k_7 \times \exp\left(-\frac{\omega}{k_8}\right) \tag{14}$$

where ω is the RS expressed in r/min, k_6 is a constant expressed in dB and represents an asymptote which physical interpretation can be thought of as $K_{intrinsic}$ averaged over the considered CFs, i.e., $k_6 = |\langle K_{intrinsic} \rangle_{CF}|_{dB}$, k_7 is a constant expressed in dB that can be physically interpreted as a measure of how much the stirring efficiency degrades at very slow RSs, whereas k_8 is a constant expressed in r/min physically interpreted as the rate at which the stirring efficiency increases as a function of the RS. An RC with a near-ideal stirring mechanism has very small k_7 and k_8. Moreover, the values of all the three fitting constants of (14) depend on the LC and the considered CF range. Additionally, according to (14), when the RS is very slow, $|\langle K \rangle_{CF}|_{dB}$ approaches $k_6 + k_7$. The physical interpretation of this low RS limit indicates the model's applicability to the considered range of RS. It is worthwhile to mention that a more sophisticated model should include the impact of the static limiting behavior. This case will then unequivocally be equivalent to no signal variation; hence, a K-factor that tends to infinity as the RS tends to zero should be expected. On the

other hand, $|\langle K \rangle_{\text{CF}}|_{\text{dB}}$ becomes approximately k_6 when the RS is fast.

After $\hat{K}$ is averaged over the considered CFs (i.e., $\langle \cdot \rangle_{\text{CF}}$) for each of the two LCs individually, it is converted into decibel, then the NLS regression method is used to fit (14) with each of the two resulted decibel-scaled averages, $\left| \left\langle \hat{K}_{\text{unloaded}} \right\rangle_{\text{CF}} \right|_{\text{dB}}$ and $\left| \left\langle \hat{K}_{\text{loaded}} \right\rangle_{\text{CF}} \right|_{\text{dB}}$. Both fits are shown in Figs. 16(a) and (b) for the unloaded and the loaded VIRC, respectively. In both LCs, the stirring efficiency degrades when decreasing the RS, which agrees with [17] and [45]. Moreover, the lower the CF range and/or the more loaded the VIRC, the larger the fitting constants of (14) become. This, in turn, results in a worse stirring efficiency (see Fig. 15), which is in accordance with [10] and [11].

3) CHANNEL GAIN

The estimated channel gain of the unloaded and the loaded VIRC are denoted by $\hat{G}_{\text{unloaded}}$ and $\hat{G}_{\text{loaded}}$, respectively. For all the considered RSs listed in Table 2, both $\hat{G}_{\text{unloaded}}$ and $\hat{G}_{\text{loaded}}$ are plotted in Fig. 17 as a function of the CF. As the figure shows, the RS has almost no impact on $\hat{G}$. This is similar to the trend in Fig. 10(b) regarding k_3 versus the RS. Moreover, the typical RC trends of a channel gain decline due to increasing the CF and/or loading [46] can also be observed in the same figure. Additionally, a clear resemblance with k_3 in Fig. 10(a) can be observed. Yet contrary to $\hat{G}$, it should be emphasized that k_3 carries no information about the unstirred component because the empirical fit of (12) exclusively takes the *stirred components* into consideration.

According to the theory [10, eq. (6)], the gain of a propagation channel inside an RC can be expressed as in

$$G = \frac{c^3 e_1 e_2}{16\pi^2 V \Delta f_{\text{mode}}} \times \frac{1}{f_c^2} \qquad (15)$$

where c is the speed of light, V is the chamber volume, Δf_{mode} is the average mode bandwidth, and e_1 and e_2 are the total efficiencies of the utilized antennas (i.e., both matching and radiation efficiencies combined). The left fraction of the expression on the right side of (15) can be averaged over the considered CFs (i.e., $\langle G f_c^2 \rangle_{\text{CF}}$) resulting in a constant denoted in decibels by k_9. Consequently, the gain of the propagation channel inside the VIRC can be empirically modeled in decibels as in

$$G_{\text{dB}} = k_9 - 20 \times \log_{10}(f_c) \qquad (16)$$

where f_c is expressed in MHz, and k_9 is a constant expressed in dBMHz^2 and whose value depends on $e_1 \times e_2$, V, and Δf_{mode}, hence the LC [10, eq. (7)]. A foundational interpretation of the physical meaning of k_9 can be obtained by evaluating (15) at $f_c = 1$ MHz. Hence, k_9 represents the reference gain of the propagation channel at 1 MHz. In general, for convenience, it can be defined depending on the frequency range at which the VIRC is evaluated, e.g., MHz or GHz.
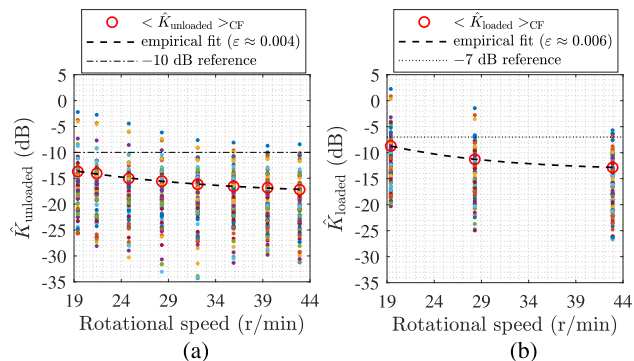

FIGURE 16. Estimated *K*-factor versus the rotational speed for (a) the unloaded and (b) the loaded VIRC. Solid lines with different colors represent the different carrier frequencies. Where ε is the coefficient of variation of the root-mean-square error between $\left| \left\langle \hat{K} \right\rangle \right|_{\text{dB}}$ and empirical fits.
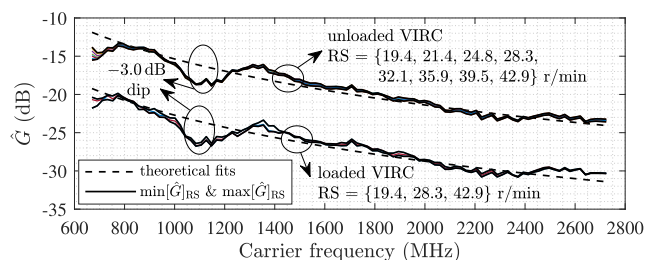

FIGURE 17. Estimated channel gain versus the carrier frequency for both loading conditions. Solid lines with different colors represent the different rotational speeds.

After $\hat{G}$ is averaged over the considered RSs (i.e., $\langle \cdot \rangle_{\text{RS}}$) for each of the two LCs individually, it is multiplied by f_c^2, averaged over the considered CFs (i.e., $\langle \cdot \rangle_{\text{CF}}$), then converted into decibel, resulting in two values for k_9 for both LCs. These two values are used to fit (16) with $\left| \left\langle \hat{G}_{\text{unloaded}} \right\rangle_{\text{RS}} \right|_{\text{dB}}$ and $\left| \left\langle \hat{G}_{\text{loaded}} \right\rangle_{\text{RS}} \right|_{\text{dB}}$. Both fits are shown in Fig. 17 which is in accordance with [46]. For the VIRC under investigation, k_9 decreases by roughly 7 dB due to loading. Moreover, a considerable deviation of up to 3 dB between the estimated channel gains and the empirical fits of (16) can be observed in the CF range 1000–1210 MHz. This is an indication that the utilized antennas have low total efficiencies within the said CF range (see (15)), which is confirmed by the matching efficiency that is less than 0.7 (see Fig. 6).

V. FURTHER INVESTIGATION AND DISCUSSION

According to [47], a 3-decibel standard deviation is the tolerance requirement of the field uniformity for CFs above 400 MHz. Moreover, the lowest usable frequency (LUF) is practically defined in [47] as the lowest frequency above which the specified field uniformity requirement is achieved for a given working volume. According to [48, Fig. 7], the LUF is roughly 600 MHz for the VIRC under investigation that is depicted in Fig. 2. This is in accordance with the observations from the previous section (see Figs. 7(a), 9(a),
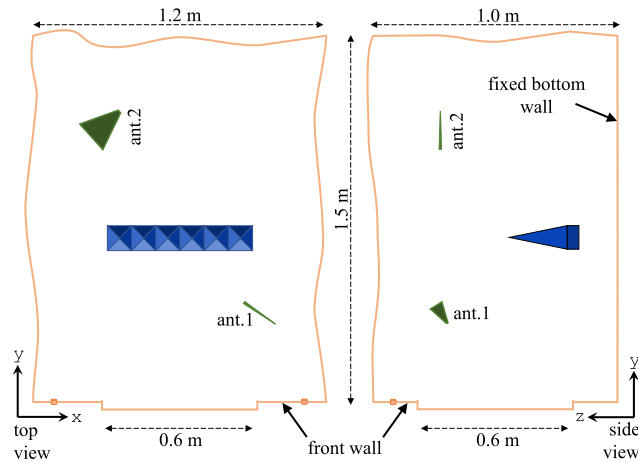
FIGURE 18. Top and side views of the layout inside the VIRC for the modified framework. Ant.1 and Ant.2 are two identical log-periodic antennas.
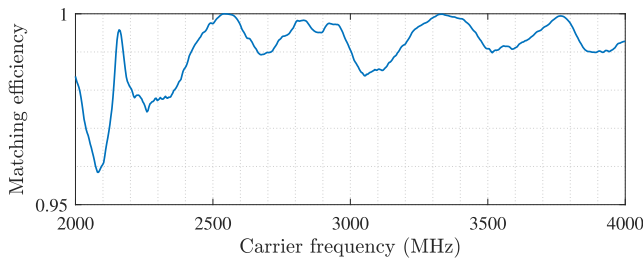

FIGURE 19. Matching efficiency of the utilized identical antennas (measured in the anechoic chamber) for the modified framework.

FIGURE 20. Estimated coherence time versus (a) the carrier frequency and (b) the rotational speed for the modified framework. The rotational speed and the carrier frequency for (a) and (b) are 39.5 r/min and 3600 MHz, respectively.

FIGURE 21. Estimated normalized frequency autocovariance function for the modified framework. Solid lines with different colors represent: (a) {2400, 3200} MHz × {24.8, 28.3, 32.1, 35.9, 39.5, 42.9} r/min and (b) {4000} MHz × {24.8, 28.3, 32.1, 35.9, 39.5, 42.9} r/min. In both (a) and (b), the empirical fit is the same and is generated using {2000, 2800, 3600} MHz ×{24.8, 28.3, 32.1, 35.9, 39.5, 42.9} r/min.

11(a), and 13(a)), in which most of the proposed models break down for CFs below 750 MHz. This can be attributed to the significant decrease in the VIRC mode density, invalidating the invoked temporal stationarity and, thereby, the temporal ergodicity in [22] for CFs below the LUF. However, for high CFs, the mode density is high enough (i.e., enough modal overlap); thereby, the invoked stationarity and the statistical method are still applicable. The consistency between the obtained estimations and the proposed models in the previous section strongly indicates the validity of the statistical method in [22] for CFs well above the LUF.

In the previous section, it has been shown that the proposed models provide good fits for the corresponding characteristics of the VIRC as long as the CF is sufficiently above the LUF. In this section, to demonstrate the generality of these models, the investigation is repeated but after adequately modifying the framework (i.e., channel and VIRC setups), as depicted in Fig. 18. First, a table is inserted beneath the VIRC to prevent its bottom wall from vibrating and, thereby, modify its stirring mechanism. Moreover, the channel setup has been modified to consider log-periodic directional antennas, a different antenna location and orientation, a different LC, and a different CF range. The matching efficiency of the utilized antennas is presented in Fig. 19 for the considered CF range. According to Figs. 20–24, the proposed models,
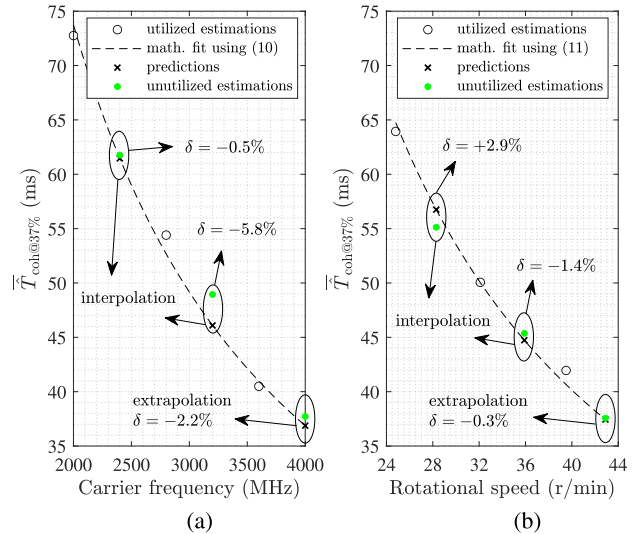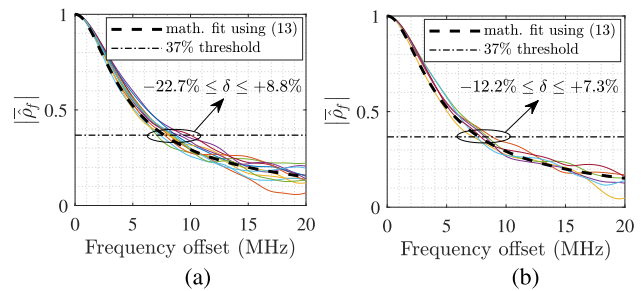
namely, (10)–(14) and (16), still provide good fits despite the substantial modification to the framework. This strongly indicates the generality of such models for comparable VIRCs.

Several fitting models, namely, (10)–(13), are required in case of developing a VIRC-based channel emulator for OTA testing as, e.g., in [11] and [49]. This is to correctly configure the VIRC variables to accurately emulate, e.g., a desired B_{coh}, T_{coh}, and $\mathcal{L}(\nu)$. In particular, the models can be used to interpolate and—to a certain degree—extrapolate the channel characteristics of the VIRC as follows. In Fig. 20(a), six CT estimations are carried out. However, based on (10), an empirical fit to the estimated CT with respect to the CF is generated only from three of the six estimations. These three estimations are referred to as "utilized estimations". The empirical fit is then used to predict the other three estimations, referred to as "unutilized estimations". Moreover, a similar approach based on (11) is applied to the estimated CT with
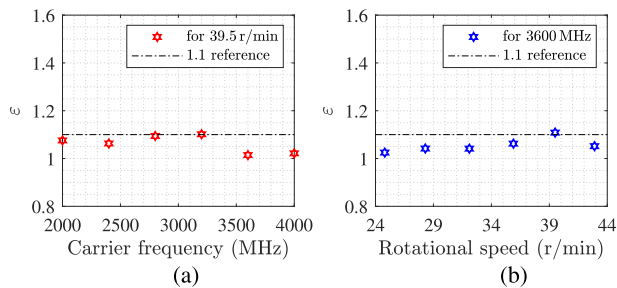
FIGURE 22. The goodness-of-fit of (12) versus (a) the carrier frequency and (b) the rotational speed for the modified framework.

FIGURE 24. Estimated channel gain versus the carrier frequency for the modified framework. Solid lines with different colors represent the rotational speeds (24.8, 28.3, 32.1, 35.9, 39.5, 42.9 r/min).
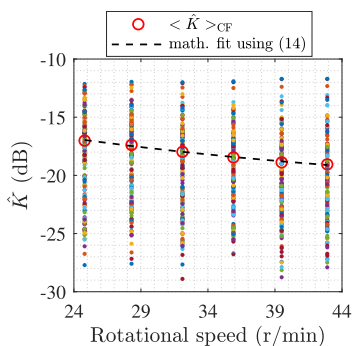

FIGURE 23. Estimated K-factor versus the rotational speed for the modified framework. Solid lines with different colors represent the carrier frequencies (2000–4000 MHz).

respect to the RS in Fig. 20(b). In all predictions, the percent error, δ, is less than 6% in absolute value. Additionally, a similar approach to Fig. 20 for the fitting constants of (12) is also applicable, yet not demonstrated due to space limitations. This can be done, however, by utilizing the trends in Figs. 10(a) and (b), which were already discussed in the previous section. Finally, a somewhat similar approach based on (13) is applied to the estimated NFAF in Fig. 21(a) and (b). In all predictions at a threshold = 37%, the percent error satisfies: $-23\% < \delta < +9\%$.

The fitting constants, k_7 and k_8, of the proposed model in (14) can be used in EMC characterization as a systematic method for evaluating the effectiveness of the stirring mechanism of different VIRCs. The smaller the constants, the less dependent the K-factor is on the RS, and the better the stirring effectiveness becomes. It is worth repeating that the K-factor depends on the shaking amplitude, which depends on the RS because of the inertia effect, as explained earlier in Section IV-C2. This dependence is conditional on the type of the implemented stirring mechanism. Generally speaking, however, given the same channel and VIRC setups (i.e., the same framework), the K-factor becomes less dependent on the RS when considering a higher CF range. In the specific case of the modified framework in Fig. 18 in comparison to the unloaded framework in Fig. 5, k_8 has almost doubled in value because of the combined effect of fixing the VIRC bottom wall and loading. This combined effect has negatively impacted the stirring efficiency. However, the net effect of the
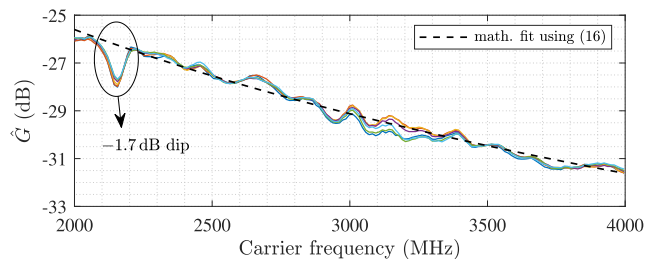
higher CF range and the utilization of directional antennas have resulted in smaller values for k_6 and k_7. This has improved the total stirring efficiency, as observed in Fig. 23 in comparison to Fig. 16(a).

According to [15] and [16], the VIRC can offer a shorter measurement time and a larger number of independent samples compared to the CLRC. Therefore, it may offer an attractive alternative for OTA-based antenna measurements conducted in CLRCs, e.g., in [6], [7], and [8]. The empirical model in (16) can be useful for preliminarily assessing the radiation efficiency of an antenna under test as long as its matching efficiency is known. This is advantageous since measuring the total efficiency using antenna positioners in anechoic chambers is expensive and time-consuming. Thanks to (16), a significant dip (i.e., deviation) below the empirical fit is an indication of low total efficiency. However, this can be attributed to either the matching efficiency, the radiation efficiency, or both. The 3-decibel dip in Fig. 17 is an example in which the dip is mainly attributed to the low matching efficiency as argued in the previous section (see Fig. 6). On the other hand, the 1.7-decibel dip in Fig. 24 is another example in which the dip is mainly attributed to the low radiation efficiency since the corresponding matching efficiency is above 0.95 (see Fig. 19).

VI. CONCLUSION

After a framework composed of channel and VIRC setups is assembled, a thorough empirical characterization of the propagation channel inside has been conducted. Various channel first- and second-order temporal and spectral characteristics have been measured, analyzed and discussed. Moreover, the effects of different rotational speeds of the VIRC motors, two loading conditions, and the frequency range 670–2740 MHz have been considered to determine the dynamic range of the studied characteristics.

For the VIRC under investigation specifically, based on $B_{\text{coh}}|_{\text{min}}$, 0.5 MHz is the maximum signaling rate of NB systems that can be tested. Furthermore, the achievable dynamic range of the Doppler spread is 4–40 Hz which corresponds to (670 MHz, 19.4 r/min, loaded)–(2740 MHz, 42.9 r/min, unloaded). Additionally, for the unloaded VIRC, the framework can provide a near-Rayleigh channel (Rician

with a K-factor below $-11\,\text{dB}$) as long as the CF is in the range 850–930 MHz or 1220–2740 MHz. For the loaded VIRC, on the other hand, the framework provides a Rician channel with a K-factor below $-7\,\text{dB}$ as long as the CF and the RS are above 840 MHz and 24.8 r/min, respectively.

Many behavioral trends have been observed while analyzing the measurement results. Consequently, several empirical models have been proposed to fit the behavior of various of these characteristics. The consistency between the models and the corresponding estimations is a strong indication of the validity of the statistical method. This is true as long as the CF is sufficiently above the LUF where the invoked stationarity is valid. Otherwise, the models break down for CFs near or below the LUF. Furthermore, the generality of the proposed models has been confirmed using a substantially modified framework. Additionally, the potential usability of these models for both EMC and OTA testing, which is to be further investigated in separate research, has been briefly demonstrated: the development of a channel emulator, the evaluation of the effectiveness of a stirring mechanism, and the assessment of the radiation efficiency of an antenna under test.

It has been found that the model of the inverse proportionality between the CT and the CF (or the RS) provides a good empirical fit. The Bell model is also an excellent practical fit for the Doppler spectrum. Furthermore, for both LCs, the model of the deviated one-sided exponential decay in (14) has been found to provide an excellent empirical fit for the decibel-scaled K-factor with respect to the RS. Moreover, the linear function model in (16) is an excellent empirical fit for the decibel-scaled channel gain with respect to the logarithmically scaled CF. Finally, considering the NFAF, it has been found that the model of the inverse-Fourier transform of the exponentially decaying pulse (i.e., (13)) provides an excellent empirical fit for both LCs.

For future research, based on the proposed fitting models and numerical results, a channel emulator for OTA testing of wireless baseband algorithms of NB SISO systems will be developed using the assembled framework described in this article. An interesting aspect to investigate will be the study of the relationship between the provided characteristics and the second-order channel characteristics, such as level crossing rate (LCR) and average fade duration (AFD), as well as their impact on system performance. Moreover, the VIRC empirical characterization and modeling will be extended to consider higher frequency bands, wideband, and multiple-input multiple-output (MIMO) channels. In the context of MIMO channels, it will be imperative to investigate the spatial properties, including the angle-of-arrival and -departure at the receiver and the transmitter, respectively. A further investigation will be conducted on the potential use of the VIRC for OTA-based antenna measurements.

REFERENCES

[1] S. Ohm, E. Kang, T. H. Lim, and H. Choo, "Design of a dual-polarization all-metal Vivaldi array antenna using a metal 3D printing method for high-power jamming systems," *IEEE Access*, vol. 11, pp. 35175–35181, 2023.

[2] M. Z. Mahfouz, A. B. J. Kokkeler, A. Meijerink, and A. A. Glazunov, "Impact of ultra-narrowband interference on Wi-Fi links: An experimental study," *IEEE Trans. Wireless Commun.*, vol. 20, no. 5, pp. 3016–3030, May 2021.

[3] A. De Leo, P. Russo, and V. M. Primiani, "Emission test method for source stirred reverberation chambers with scalar measurements," *IEEE Access*, vol. 11, pp. 16749–16756, 2023.

[4] A. Hussain, P. Kildal, and A. A. Glazunov, "Interpreting the total isotropic sensitivity and diversity gain of LTE-enabled wireless devices from over-the-air throughput measurements in reverberation chambers," *IEEE Access*, vol. 3, pp. 131–145, 2015, doi: 10.1109/ACCESS.2015.2411393.

[5] X. Chen, P.-S. Kildal, and M. Gustafsson, "Characterization of implemented algorithm for MIMO spatial multiplexing in reverberation chamber," *IEEE Trans. Antennas Propag.*, vol. 61, no. 8, pp. 4400–4404, Aug. 2013.

[6] C. L. Holloway, H. A. Shah, R. J. Pirkl, W. F. Young, D. A. Hill, and J. Ladbury, "Reverberation chamber techniques for determining the radiation and total efficiency of antennas," *IEEE Trans. Antennas Propag.*, vol. 60, no. 4, pp. 1758–1770, Apr. 2012.

[7] A. Hubrechsen, K. A. Remley, R. D. Jones, D. F. Williams, D. Gu, A. B. Smolders, and L. A. Bronckers, "The effect of noise on reverberation-chamber measurements of antenna efficiency," *IEEE Trans. Antennas Propag.*, vol. 69, no. 12, pp. 8744–8752, Dec. 2021.

[8] W. Xue, X. Chen, M. Zhang, L. Zhao, A. Zhang, and Y. Huang, "Statistical analysis of antenna efficiency measurements with non-reference antenna methods in a reverberation chamber," *IEEE Access*, vol. 8, pp. 113967–113980, 2020.

[9] V. M. Primiani, M. Barazzetta, L. Bastianelli, D. Micheli, F. Moglie, R. Diamanti, and G. Gradoni, "Reverberation chambers for testing wireless devices and systems," *IEEE Electromagn. Compat. Mag.*, vol. 9, no. 2, pp. 45–55, 2nd Quart., Jul. 2020.

[10] P.-S. Kildal, X. Chen, C. Orlenius, M. Franzen, and C. S. L. Patane, "Characterization of reverberation chambers for OTA measurements of wireless devices: Physical formulations of channel matrix and new uncertainty formula," *IEEE Trans. Antennas Propag.*, vol. 60, no. 8, pp. 3875–3891, Aug. 2012.

[11] C. L. Holloway, D. A. Hill, J. M. Ladbury, P. F. Wilson, G. Koepke, and J. Coder, "On the use of reverberation chambers to simulate a Rician radio environment for the testing of wireless devices," *IEEE Trans. Antennas Propag.*, vol. 54, no. 11, pp. 3167–3177, Nov. 2006.

[12] X. Chen, J. Tang, T. Li, S. Zhu, Y. Ren, Z. Zhang, and A. Zhang, "Reverberation chambers for over-the-air tests: An overview of two decades of research," *IEEE Access*, vol. 6, pp. 49129–49143, 2018.

[13] J. Yousaf, W. Nah, M. I. Hussein, J. G. Yang, A. Altaf, and M. Elahi, "Characterization of reverberation chamber—A comprehensive review," *IEEE Access*, vol. 8, pp. 226591–226608, 2020.

[14] F. Leferink, J.-C. Boudenot, and W. van Etten, "Experimental results obtained in the vibrating intrinsic reverberation chamber," in *Proc. IEEE Int. Symp. Electromagn. Compatibility. Symp. Rec.*, Aug. 2000, pp. 639–644.

[15] G. Andrieu, N. Meddeb, C. Jullien, and N. Ticaud, "Complete framework for frequency and time-domain performance assessment of vibrating intrinsic reverberation chambers," *IEEE Trans. Electromagn. Compat.*, vol. 62, no. 5, pp. 1911–1920, Oct. 2020.

[16] R. Vogt-Ardatjew, "Electromagnetic fields in reverberant environments," Ph.D. dissertation, Faculty Elect. Eng., Math. Comput. Sci. (EEMCS), Univ. Twente, Enschede, The Netherlands, 2017, doi: 10.3990/1.9789036544245.

[17] M. Hara, Y. Takahashi, R. Vogt-Ardatjew, and F. Leferink, "Statistical analysis for reverberation chamber with flexible shaking walls with various amplitudes," in *Proc. Int. Symp. Electromagn. Compat.*, Aug. 2018, pp. 694–698.

[18] G. Ferrara, A. Gifuni, M. Migliaccio, and A. Sorrentino, "Probability density function for the quality factor of vibrating reverberation chambers," *IEEE Metrol. Aerosp.*, pp. 230–234, Jun. 2015, doi: 10.1109/MetroAeroSpace.2015.7180659.

[19] R. Vogt-Ardatjew, S. van de Beek, and F. Leferink, "Influence of reverberation chamber loading on extreme field strength," in *Proc. Int. Symp. Electromagn. Compat., Tokyo*, May 2014, pp. 685–688.

[20] R. Vogt-Ardatjew, S. van de Beek, and F. Leferink, "Experimental extreme field strength investigation in reverberant enclosures," in *Proc. Int. Symp. Electromagn. Compat.*, Sep. 2014, pp. 332–336.

[21] R. Vogt-Ardatjew and F. Leferink, "Observation of maximal and average field values in a reverberation chamber," in *Proc. Int. Symp. Electromagn. Compat.*, Sep. 2013, pp. 508–513.

[22] M. Z. Mahfouz, R. Vogt-Ardatjew, A. B. J. Kokkeler, and A. A. Glazunov, "Measurement and estimation methodology for EMC and OTA testing in the VIRC," *IEEE Trans. Electromagn. Compat.*, vol. 65, no. 1, pp. 3–16, Feb. 2023.

[23] M. Z. Mahfouz, "Ultra-narrowband communications: A feasibility study for the 2.4 GHz band," Ph.D. dissertation, Faculty Elect. Eng., Math. Comput. Sci. (EEMCS), Univ. Twente, Enschede, The Netherlands, Sep. 2023, doi: 10.3990/1.9789036557900.

[24] R. J. Pirkl, K. A. Remley, and C. S. L. Patane, "Reverberation chamber measurement correlation," *IEEE Trans. Electromagn. Compat.*, vol. 54, no. 3, pp. 533–545, Jun. 2012.

[25] T. S. Rappaport, *Wireless Communications: Principles and Practice*, 2nd ed. Upper Saddle River, NJ, USA: Prentice-Hall, 2002.

[26] A. Sorrentino, A. Gifuni, G. Ferrara, and M. Migliaccio, "Mode-stirred reverberating chamber Doppler spectra: Multi-frequency measurements and empirical model," *IET Microwave Antennas Propag.*, vol. 8, no. 15, pp. 1356–1362, Dec. 2014.

[27] C. Lemoine, P. Besnier, and M. Drissi, "Investigation of reverberation chamber measurements through high-power goodness-of-fit tests," *IEEE Trans. Electromagn. Compat.*, vol. 49, no. 4, pp. 745–755, Nov. 2007.

[28] W. Rolke and C. G. Gongora, "A chi-square goodness-of-fit test for continuous distributions against a known alternative," *Comput. Statist.*, vol. 36, no. 3, pp. 1885–1900, Sep. 2021, doi: 10.1007/s00180-020-00997-x.

[29] M. A. Stephens, "EDF statistics for goodness of fit and some comparisons," *J. Amer. Stat. Assoc.*, vol. 69, no. 347, pp. 730–737, Sep. 1974, doi: 10.1080/01621459.1974.10480196.

[30] A. Gifuni, L. Bastianelli, M. Migliaccio, F. Moglie, V. Mariani Primiani, and G. Gradoni, "On the estimated measurement uncertainty of the insertion loss in a reverberation chamber including frequency stirring," *IEEE Trans. Electromagn. Compat.*, vol. 61, no. 5, pp. 1414–1422, Oct. 2019.

[31] V. Erceg, *TGn Channel Models*, document 802.11-40r4, May 2004.

[32] M. Jeong, B.-Y. Park, J. Choi, and S.-O. Park, "Doppler spread spectrum of a circularly moving receiver in an anechoic and a reverberation chamber," *Prog. Electromagn. Res. C*, vol. 48, pp. 125–132, 2014.

[33] X. Chen, "Evaluation and measurement of the Doppler spectrum in a reverberation chamber," *Prog. Electromagn. Res. M*, vol. 26, pp. 267–277, 2012.

[34] J.-H. Choi, J.-H. Lee, and S.-O. Park, "Characterizing the impact of moving mode-stirrers on the Doppler spread spectrum in a reverberation chamber," *IEEE Antennas Wireless Propag. Lett.*, vol. 9, pp. 375–378, 2010.

[35] Z. Tian, Y. Huang, and Q. Xu, "Stirring effectiveness characterization based on Doppler spread in a reverberation chamber," in *Proc. 10th Eur. Conf. Antennas Propag. (EuCAP)*, Apr. 2016, pp. 1–3.

[36] T. Tank and J.-P.-M. G. Linnartz, "Statistical characterization of Rician multipath effects in a mobile-to-mobile communication channel," *Int. J. Wireless Inf. Netw.*, vol. 2, no. 1, pp. 17–26, Jan. 1995, doi: 10.1007/bf01464195.

[37] A. S. Akki and F. Haber, "A statistical model of mobile-to-mobile land communication channel," *IEEE Trans. Veh. Technol.*, vol. VT-35, no. 1, pp. 2–7, Feb. 1986.

[38] D. A. Hill, "Electromagnetic theory of reverberation chambers," in *Dept. Radio-Freq. Technol. DivisionElectron. Elect. Eng. Lab. Natl. Inst. Stand. Technol.*, Nov. 1998, p. 60, doi: 10.6028/nist.tn.1506.

[39] E. Genender, C. L. Holloway, K. A. Remley, J. M. Ladbury, G. Koepke, and H. Garbe, "Simulating the multipath channel with a reverberation chamber: Application to bit error rate measurements," *IEEE Trans. Electromagn. Compat.*, vol. 52, no. 4, pp. 766–777, Nov. 2010.

[40] X. Chen, P.-S. Kildal, C. Orlenius, and J. Carlsson, "Channel sounding of loaded reverberation chamber for over-the-air testing of wireless devices: Coherence bandwidth versus average mode bandwidth and delay spread," *IEEE Antennas Wireless Propag. Lett.*, vol. 8, pp. 678–681, 2009.

[41] M. I. Andries, P. Besnier, and C. Lemoine, "On the prediction of the average absorbing cross section of materials from coherence bandwidth measurements in reverberation chamber," in *Proc. Int. Symp. Electromagn. Compat. EMC Eur.*, Sep. 2012, pp. 1–6.

[42] G. Orjubin, E. Richalot, S. Mengue, and O. Picon, "Statistical model of an undermoded reverberation chamber," *IEEE Trans. Electromagn. Compat.*, vol. 48, no. 1, pp. 248–251, Feb. 2006.

[43] C. Lemoine, P. Besnier, and M. Drissi, "Effect of the size of the antenna on measurements distribution in reverberation chamber," in *Proc. 18th Int. Zurich Symp. Electromagn. Compat.*, Sep. 2007, pp. 461–464.

[44] L. L. Bars, J.-F. Rosnarho, P. Besnier, J. Sol, F. Sarrazin, and E. Richalot, "Geometry and loading effects on performances of mode-stirred reverberation chambers: An experimental study," in *Proc. Int. Symp. Electromagn. Compat. MC Eur.*, Sep. 2019, pp. 163–168.

[45] M. Hara, Y. Takahashi, R. Vogt-Ardatjew, and F. Leferink, "Validation of vibrating intrinsic reverberation chamber using computational electromagnetics," in *Proc. Joint Int. Symp. Electromagn. Compat., Sapporo Asia–Pacific Int. Symp. Electromagn. Compat.*, Jun. 2019, pp. 593–596.

[46] U. Carlberg, P.-S. Kildal, and J. Carlsson, "Numerical study of position stirring and frequency stirring in a loaded reverberation chamber," *IEEE Trans. Electromagn. Compat.*, vol. 51, no. 1, pp. 12–17, Feb. 2009.

[47] *Electromagnetic Compatibility (EMC), Part 4–21: Testing and Measurement Techniques-Reverberation Chamber Test Methods*, IEC Standard 61000-4-21, Int. Electrotechnical Commission, Geneva, Switzerland, 2011.

[48] D. Mandaris, R. Vogt-Ardatjew, E. Suthau, and F. Leferink, "Simultaneous multi-probe measurements for rapid evaluation of reverberation chambers," in *Proc. IEEE Int. Symp. Electromagn. Compat. IEEE Asia–Pacific Symp. Electromagn. Compat. (EMC/APEMC)*, May 2018, pp. 590–594.

[49] A. B. Kihero, M. Karabacak, and H. Arslan, "Emulation techniques for small scale fading aspects by using reverberation chamber," *IEEE Trans. Antennas Propag.*, vol. 67, no. 2, pp. 1246–1258, Feb. 2019.

MHD ZAHER MAHFOUZ received the B.Sc. degree in electronics and communications engineering from Damascus University, Damascus, Syria, in 2011, the M.Sc. degree in electrical-electronics and telecommunications engineering from University Technology Malaysia, Johor Bahru, Malaysia, in 2014, and the Ph.D. degree in electrical engineering from the University of Twente, Enschede, The Netherlands, in 2023.

In May 2012, he did a three-month traineeship with RF Section (RNO-GSM & GPRS), Huawei Company Ltd., Syria Branch. In December 2014, he joined the UTM MIMOS Center of Excellence, as an Assistant Research Officer, for half a year. In July 2015, he was a Ph.D. Researcher with the Telecommunication Engineering (TE) Group, Slow Wireless Project, University of Twente. In August 2018, he did a research visit for five months with Gapwaves AB, Göteborg, Sweden, during which he worked on MIMO antenna array characterization in RIMP and RLOS channel models. He is currently a Lecturer with the Radio Systems Group, University of Twente. His research interests include PHY of wireless sensor networks, wireless co-existence, and channel measurements, characterization and emulation.

ROBERT VOGT-ARDATJEW (Member, IEEE) received the M.Sc. degree in electronics and telecommunications from the Wroclaw University of Science and Technology, Wroclaw, Poland, in 2011, and the Ph.D. degree in electrical engineering from the University of Twente, Enschede, The Netherlands, in 2017.

He is currently an Assistant Professor with the Power Electronics and Electromagnetic Compatibility Group, University of Twente. His research interests include electromagnetic field measurements and analysis, reverberation chambers, and their applications in electromagnetic compatibility.

ANDRÉ B. J. KOKKELER (Member, IEEE) received the Ph.D. degree in computer science from the University of Twente, Enschede, The Netherlands, in 2005.

He worked more than six years with Ericsson, as a System Engineer, and eight years with the Netherlands Foundation for Research in Astronomy (ASTRON), as a Scientific Project Manager. In 2003, he joined the University of Twente, where he is currently a Full Professor and the Chair of the Radio Systems Group. He has a background in telecommunication, mixed signal design, and signal processing architectures. He is involved in research projects, sponsored by the Dutch and European governments and industry. His research interests include the design of low-power architectures for telecommunications and computationally intensive applications, with a focus on efficient realization of digital signal processing for communications.

ANDRÉS ALAYÓN GLAZUNOV (Senior Member, IEEE) was born in Havana, Cuba. He received the M.Sc. (Engineer-Researcher) degree in physical engineering from Peter the Great St. Petersburg Polytechnic University (Polytech), Saint Petersburg, Russia, in 1994, the Ph.D. degree in electrical engineering from Lund University, Lund, Sweden, in 2009, and the Docent (Habilitation) degree in antenna systems from the Chalmers University of Technology, Gothenburg, Sweden, in 2017.

From 1996 to 2005, he held various research and specialist positions with the telecom industry, e.g., Ericsson Research, Telia Research, and TeliaSonera; Stockholm, Sweden. From 2001 to 2005, he was the Swedish Delegate with the European Cost Action 273, and from 2018 to 2020, he was the Dutch Delegate with the European Cost Action IRACON. He has been one of the pioneers in producing the first standardized OTA measurement techniques for 3GPP, and devising novel OTA techniques, e.g., the random-LOS and the hybrid antenna characterization setups. He has contributed to, or initiated various European research projects, e.g., more recently, is3DMIMO, WAVECOMBE, 5VC, and Build-Wise projects under the auspices of the H2020 European Research and Innovation Program. He also contributed to the international 3GPP and the ITU standardization bodies. From 2009 to 2010, he held a Marie Curie Senior Research Fellowship with the Centre for Wireless Network Design, University of Bedfordshire, Luton, U.K. From 2010 to 2014, he held a postdoctoral position with the Electromagnetic Engineering Laboratory, KTH-Royal Institute of Technology, Stockholm. From 2014 to 2018, he was an Assistant Professor with the Chalmers University of Technology. From 2018 to 2023, he was an Associate Professor with the Department of Electrical Engineering, University of Twente, Enschede, The Netherlands. He is currently a Senior Associate Professor with the Department of Science and Technology, Linköping University, Norrköping, Sweden. He is the author of more than 150 scientific and technical publications. He is the coauthor and the coeditor of the text book *LTE-Advanced and Next Generation Wireless Networks-Channel Modelling and Propagation* (Wiley, 2012). His current research interests include, but are not limited to, mmWave array antenna design, MIMO antenna systems, electromagnetic theory, fundamental limitations on antenna-channel interactions, radio propagation channel measurements, modeling and simulations, wireless performance in the built environment, and the OTA characterization of antenna systems and wireless devices for communication and sensing.

・・・